International Global Navigation Satellite Systems Association
IGNSS Symposium 2020

Colombo Theatres, Kensington Campus, UNSW Australia
5 – 7 February 2020

Evaluation of integrity availability based on classic RAIM in different urban environments for stand-alone GPS and multi-sensor solutions

Jelena Gabela
Department of Electrical and Electronic Engineering, The University of Melbourne, Australia
jgabela@student.unimelb.edu.au

Allison Kealy
Department of Geospatial Science, RMIT University, Australia
allison.kealy@rmit.edu.au

Xavier Bachelet
Research and Development (R&D) Department, Amphenol Antenna Solutions, France
xbachelet@amphenol-antennas.com

William Moran
Department of Electrical and Electronic Engineering, The University of Melbourne, Australia
wmoran@unimelb.edu.au

Mark Hedley
CSIRO, Data 61, Sydney, Australia
Mark.Hedley@data61.csiro.au

ABSTRACT

This paper aims to demonstrate the possible effects of different types of the urban environment (i.e., highway, urban canyons, suburb, and open-sky areas) on integrity monitoring of a positioning system based on stand-alone Global Navigation Satellite System (GNSS) solution. In addition to that, capabilities and possible improvements with the addition of a Local Positioning System (LPS) are explored. The effect of the environment is tested on the integration of the Extended Kalman Filter (EKF) for Weighted Least Squares (WLS) Receiver Autonomous Integrity Monitoring (RAIM) algorithm for GPS data, collected for one vehicle in August of 2018 in Melbourne, Australia. Capabilities of multi-sensor RAIM algorithm will be tested on the collected GPS data, and on simulated ranging data to LPS anchors. The results demonstrate that in areas like suburbs and urban canyons, under conditions of alarm limit of 20 m and integrity risk of $1 \cdot 10^{-5}$, integrity is not available. On the highway, the integrity is available approximately 73% of the time. With the addition of the LPS data, integrity availability estimates improve in all environments. Integrity in urban canyon and suburban environments becomes available 75% and 80% of the time,

respectively. The integrity availability in open-sky areas and highway increases to 100%.

KEYWORDS: EKF, GNSS, Local Positioning System - LPS, Multi-sensor fusion, RAIM.

1. INTRODUCTION

Integrity can be defined as the "ability of the system to provide timely warnings to users when the system should not be used for navigation" (Brown, 1988). This definition was specified by the Integrity Working Group which was formed in 1986 by Radio Technical Commission for Aeronautics Special Committee-159, in order to help with determining the integrity monitoring requirements and to discuss the integrity monitoring methods for civil aviation. Given the safety implications of civil aviation, it was necessary to have a standard that clearly defines the required performance. Recently, with the development of Intelligent Transport Systems (ITS), a lot of effort has been put into developing the integrity monitoring for land-based applications. However, there is a lack of agreement on integrity requirements for such applications which probably stems from the application and environment diversity. European GNSS Agency report from 2015 (see References) defines integrity requirements for three classes of applications: safety-critical applications (e.g., autonomous driving), payment-critical applications (e.g., tolling), and regulatory-critical applications (e.g., emergency services). For each application, four requirements are defined: integrity risk, continuity risk, Alarm Limit (AL) and time to alarm. This paper will focus on integrity risk and AL. European GNSS Agency (2015) defines integrity risk as probability that at any moment, position error (PE) will exceed the Protection Level (PL) estimated by the integrity algorithm. PL is defined as an interval which is assured to contain the PE with the probability of failure equal to integrity risk. AL is an interval that is required to contain the PE. If this is not true, the alarm should be raised. Thus, integrity is available if $PE < PL < AL$.

A lot of the research in the integrity monitoring for land-based applications has been based on implementations of the algorithms originally developed for civil aviation (Kealy *et al.*, 2015; Zhu *et al.*, 2018). One of those algorithms is Receiver Integrity Monitoring Algorithm (RAIM), which relies on a statistical characterisation of the pseudorange residuals (European GNSS Agency, 2015). The biggest disadvantage of implementing the RAIM in urban environments is its dependence on the availability of measurements, especially if only the Global Navigation Satellite System (GNSS) data are used. This disadvantage is problematic in the urban environments where the measurement availability and quality of the GNSS data can be severely affected.

This paper will demonstrate the effects of the different types of the environment on integrity availability for GNSS data. Integrity will be estimated using the classic snap-shot Weighted Least Squares (WLS) RAIM with the Extended Kalman Filter (EKF) as the underlying positioning framework in an open-sky environment, on a highway, in a suburban area and in the urban canyon area. Given the results in Salós *et al.* (2014) and Tran and Lo Presti (2019) where different RAIM algorithms have been tested in different environments on GNSS data, the hypothesis of this paper is that integrity availability will decrease as the environment types are becoming more complex and challenging. Unlike Tran and Lo Presti (2019) where a change of Horizontal PL (HPL) has been studied, this paper will also analyse the integrity in terms of availability for a specific application class. Furthermore, a case study will be carried out on multiple environments and detailed analysis of the environment effects will be made.

Finally, to mitigate the effect of the urban environment on the GNSS data, the capabilities and possible improvements of position estimation and integrity will be tested on a multi-sensor fusion system. The real-world GNSS data will be fused with the simulated Local Positioning System (LPS) relative ranges. It is expected that LPS data will be able to improve overall measurement availability and thus the integrity availability. Although a lot of research has been done in the area of the multi-sensor integrity monitoring algorithms, the majority is based on the fusion of GNSS and Inertial Measurement Units. However, there are examples of research where different multi-sensor algorithms have been developed (El-Mowafy and Kubo, 2017; El-Mowafy and Kubo, 2018; Shytermeja et al., 2014).

The aim of this paper is to demonstrate the effect of different environments on integrity availability, identify the biggest drawbacks of implementing RAIM-like methods for land-based vehicle applications and to mitigate the environment effect on integrity estimate by employing the multi-sensor positioning system. This following section provides an overview of the experimental setup followed by the mathematical framework section where EKF and WLS RAIM have been defined. The results of the implementation of said algorithms are presented in Section 4 which is followed by the conclusion.

2. EXPERIMENT SETUP

Experiments shown in this paper have been performed on real-world GNSS data collected in Melbourne, Australia in July 2018. As one of the aims of the paper is to demonstrate the possible effects of different types of the environment on the performance of the WLS RAIM algorithm, the data used in the experiments were collected in four different environments: highway, open-sky, urban/suburban and urban canyon. In addition to this, the integrity performance is tested for a static vehicle in open-sky conditions. Open-sky, suburb and urban canyon areas were chosen due to expectedly different satellite visibility. The highway was chosen so that the performance of EKF and RAIM can be tested when the vehicle is moving with high speed. Figures 1a-4a are showing the trajectories of the vehicles in all four environments. It should be noted that Figure 1a, shows the location where the static vehicle data were collected in the open-sky environment (blue mark). The highest achieved velocity is just under 100 km/h (Figure 1b). Velocities of the vehicle in all environments are shown in Figures 1b-4b.

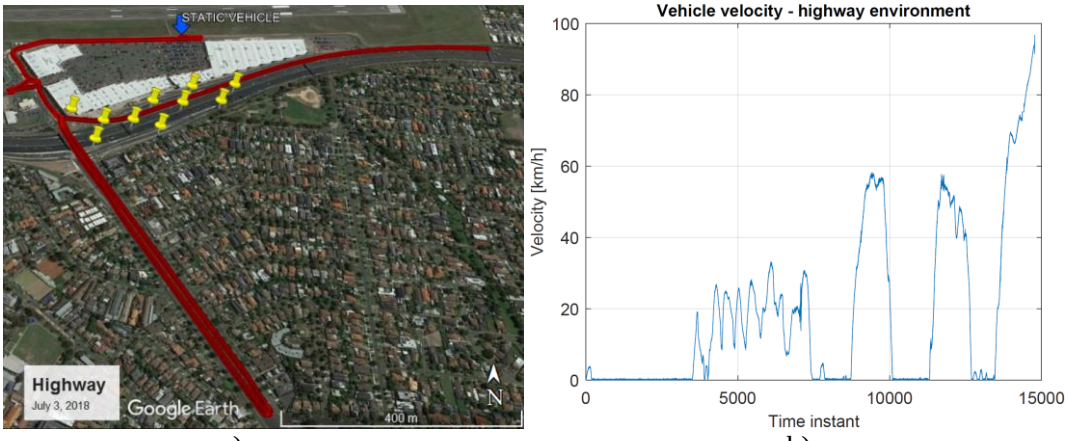

a) b)

Figure 1. a) The trajectory of the vehicle on the highway (Citylink) with Google Earth satellite image as a base map. b) The velocities reached by the vehicle.

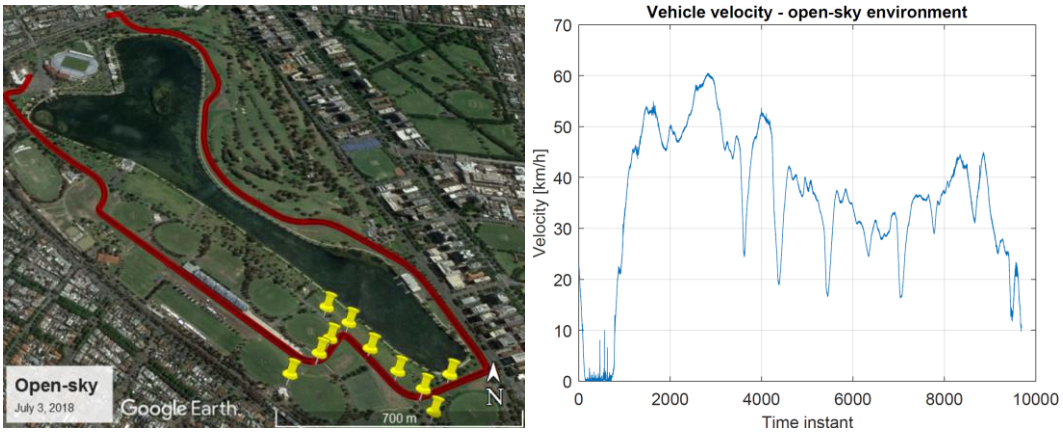

a) b)

Figure 2. a) The trajectory of the vehicle in the open-sky environment (Albert Park) with Google Earth satellite image as a base map. b) The velocities reached by the vehicle.

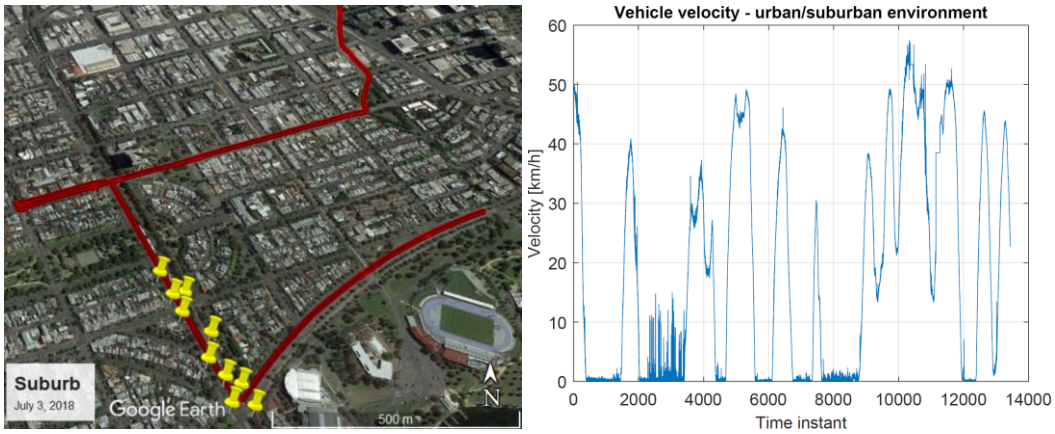

a) b)

Figure 3. a) The trajectory of the vehicle in the urban/suburban environment (South Melbourne) with Google Earth satellite image as a base map. b) The velocities reached by the vehicle.

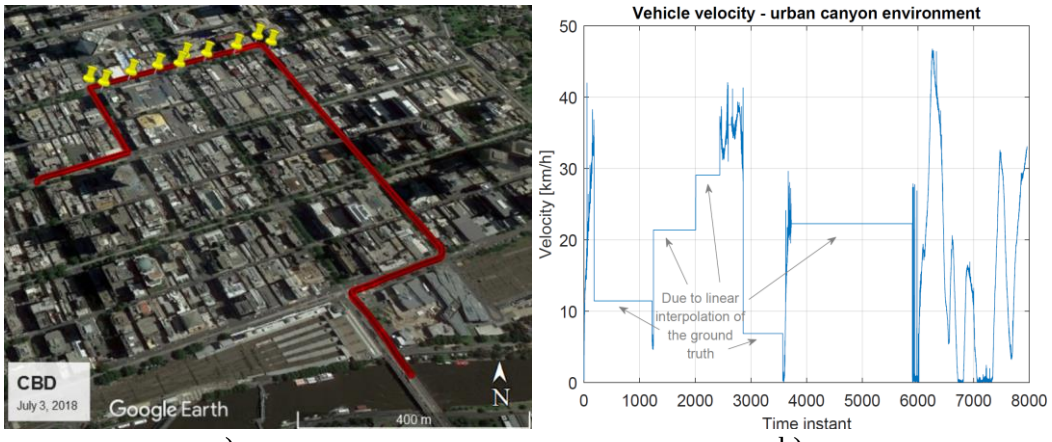

a) b)

Figure 4. a) The trajectory of the vehicle in the urban canyon (Melbourne Central Business District) with Google Earth satellite image as a base map. b) The velocities reached by the vehicle.

To test the potential capabilities of the integration of GPS and LPS (i.e., multi-sensor), the LPS data (i.e., relative ranges) are simulated on subsets of the shown trajectories. Anchor nodes (yellow pins in Figures 1a-4a) are set up around the road segments. The relative

ranging data between the vehicle and the anchors are simulated with added zero-mean Gaussian noise with standard deviation *1 m*.

GNSS data were collected using the surveying grade Leica GNSS receiver. The receiver was mounted on the vehicle using the magnetic mount. More information about the used receiver can be found in Leica Geosystems AG data sheet (URL provided in References). Although the data from GLONASS and Galileo were collected as well, only GPS code pseudoranges, uncorrected for atmospheric effects, were used as the measurements. Post-processed dual-frequency GPS data in addition to the data from Continuously Operating Reference Station (CORS) in Melbourne (i.e., MOBS) were used as the ground truth for integrity and accuracy assessment. The RTKLib open-source software package was used to determine the ground truth with the precision at a sub-centimetre level. During a big portion of the data collection in the urban canyon and at some instances in the suburban environment, when less than four measurements were available, it was not possible to determine the ground truth with sub-centimetre precision. Thus, given the linearity of the road segments where this occurs, linear interpolation was used to derive the ground truth positions. Further, when interpolating the positions, constant velocity is assumed (as shown in Figure 4b).

3. MATHEMATICAL FRAMEWORK

The positioning framework is based on the general cooperative positioning EKF presented in Gabela *et al.* (2018) and multi-sensor EKF presented in Gabela *et al.* (2019). Furthermore, the RAIM method used in this paper is based on Bruckner (2010).

3.1 Positioning framework

This section presents a multi-sensor positioning framework based on the EKF. Pseudorange (i.e., GNSS satellite measurements) and relative range (i.e., measurements to the LPS) measurements are being fused. Thus, a network of N_I LPS anchors (i.e., infrastructure nodes) and a network of N_S GNSS satellites are considered. The positions of the GNSS satellites are predicted using the ephemeris data and are determined in ECEF (Earth-Centred, Earth-Fixed) frame. The positions of the anchors are assumed to have been precisely determined in ECEF frame as well. The position r_k of the vehicle or a different type of road user is estimated within the state vector X_k at a time instant k. In addition to the 3D position, 3D velocity v_k, 3D acceleration a_k and user clock bias c_b^k in units of length (obtained by multiplying clock bias with the speed of light) are all estimated within the X_k.

$$X_k = \begin{bmatrix} r_k & v_k & a_k & c_b^k \end{bmatrix}^T \tag{1}$$

Although the presented framework is estimating the 3D positions of the user, by removing the third dimension of the position, velocity, and acceleration in the state vector, the algorithm can be altered to estimate 2D positions, 2D velocity, and 2D acceleration. However, it should be noted that in the case of the fusion of pseudoranges and relative ranges, 3D ranges are usually measured and without angle measurements, it is not possible to reduce them to 2D ranges. In this paper, the measurement vector Z_k consists of pseudorange measurements

vector ρ_k and relative range measurement vector d_k.

$$\underset{(N_I+N_S)\times 1}{Z_k} = \begin{bmatrix} \underset{1\times N_S}{\rho_k} & \underset{1\times N_I}{d_k} \end{bmatrix}^T \tag{2}$$

The user's state evolution is expressed with

$$\begin{aligned} X_k &= f\left(X_{k-1}, \omega_k\right) \\ \omega_k &\sim N\left(0, Q_k\right) \end{aligned}, \tag{3}$$

where X_{k-1} denotes previously estimated state at a time instant $k-1$. ω_k denotes the process noise which is assumed to be zero-mean Gaussian with variance matrix Q_k. In this paper, the variance matrix consists of the acceleration and GNSS receiver clock bias process noise. $f(\cdot)$ denotes a state evolution function governed by the state transition functions

$$\begin{aligned} \dot{r} &= v \\ \dot{v} &= a \end{aligned}. \tag{4}$$

$\dot{r}$ denotes the rate of change of position which equals velocity v, and $\dot{v}$ denotes rate of change of velocity which equals acceleration a. In this case, the state evolution model is a constant acceleration model. Thus, the transition matrix F_k is defined as

$$F_k = \begin{bmatrix} \underset{3\times 3}{I} & \underset{3\times 3}{I\cdot\delta t} & \underset{3\times 3}{\frac{1}{2}I\,\delta t^2} & \underset{3\times 1}{0} \\ \underset{3\times 3}{0} & \underset{3\times 3}{I} & \underset{3\times 3}{I\,\delta t} & \underset{3\times 1}{0} \\ \underset{3\times 3}{0} & \underset{3\times 3}{0} & \underset{3\times 3}{I} & \underset{3\times 1}{0} \\ \underset{1\times 3}{0} & \underset{1\times 3}{0} & \underset{1\times 3}{0} & 1 \end{bmatrix}, \tag{5}$$

where I is an identity matrix with dimensions specified under the symbol and δt is a time increment between two states. The measurement model is expressed as

$$\begin{aligned} Z_k &= h\left(X_k\right) + u_k \\ u_k &= \begin{bmatrix} \xi_k & \varsigma_k \end{bmatrix}^T \\ \xi_k &\sim N\left(0, \sigma_S^2\right) \\ \varsigma_k &\sim N\left(0, \sigma_I^2\right) \end{aligned}. \tag{6}$$

u_k is a measurement noise vector which consists of pseudorange measurement noise ξ_k and relative range measurement noise ς_k. Both are assumed to be zero-mean Gaussian with standard deviations σ_S^2 and σ_I^2, respectively. $h(\cdot)$ denotes a general non-linear measurement function. In this case, the measurement model consists of two non-linear functions

$$\begin{aligned}\rho_k^i &= \sqrt{\left(x_S^i - x_k\right)^2 + \left(y_S^i - y_k\right)^2 + \left(z_S^i - z_k\right)^2} + c_{b(k)}^i + \xi_k^i \\ d_k^j &= \sqrt{\left(x_I^j - x_k\right)^2 + \left(y_I^j - y_k\right)^2 + \left(z_I^j - z_k\right)^2} + \varsigma_k^j\end{aligned}, \tag{7}$$

where ρ_k^i and d_k^i denote the pseudorange and relative range measurements, respectively. $(x, y, z)_k$ denotes the predicted user's position. $(x_S, y_S, z_S)_k^i$ is the ECEF position of the i^{th} satellite where $i \in 1, \ldots, N_S$ at time instant k. $(x_I, y_I, z_I)^j$ is the ECEF position of the j^{th} anchor node where $j \in 1, \ldots, N_I$ at time instant k. The first-order Taylor series expansion is used to approximate the non-linear measurement model. Jacobian matrices for the i^{th} and the j^{th} satellite and anchor are given below, as well as the measurement matrix H_k which consists of all the individual Jacobian matrices.

$$\begin{aligned}H_k^{\rho_i} &= \begin{bmatrix} \underset{1\times3}{\dfrac{\partial \rho_k^i}{\partial r_k}} & \underset{1\times3}{0} & \underset{1\times3}{0} & \underset{1\times1}{1} \end{bmatrix} \\ H_k^{d_j} &= \begin{bmatrix} \underset{1\times3}{\dfrac{\partial d_k^j}{\partial r_k}} & \underset{1\times3}{0} & \underset{1\times3}{0} & \underset{1\times1}{0} \end{bmatrix} \\ \underset{(N_S+N_I)\times10}{H_k} &= \begin{bmatrix} H_k^{\rho_1} & \cdots & H_k^{\rho_{N_S}} & H_k^{d_1} & \cdots & H_k^{d_{N_I}} \end{bmatrix}^T\end{aligned} \tag{8}$$

Presented matrices are defined for a multi-sensor solution where GNSS data and LPS data are fused. However, in the case of stand-alone GNSS EKF, rows in Z_k, u_k and H_k related to relative ranges would be removed. For stand-alone LPS data, all rows in the same matrices relating to the GNSS measurements would be removed. The standard EKF equations can be used to estimate the user's state.

2.2 HPL calculation

This section presents the RAIM used to estimate the HPL, adapted based on the Bruckner (2010). Smith *et al.* (2018) uses this algorithm as well and presents it in a more condensed form. In this paper variables used to calculate HPL value are provided by the EKF. The HPL can be calculated as follows

$$HPL = K_{ffmd} d_{major}. \tag{9}$$

K_{ffmd} is a missed detection multiplier which is defined using the required Integrity Risk p_{IR}.

$$K_{ffmd} = -\sqrt{2} \cdot erfcinv\left(2 \cdot \left(1 - \frac{1 - p_{IR}}{2}\right)\right) \tag{10}$$

erfcinv denotes the inverse complementary error function. This parameter stays constant for the duration of the experiment. d_{major} denotes the 1σ standard deviation of the position that is

to be estimated in the direction of the major axis of the error ellipse. This is would be the worst-case horizontal error. d_{major} is calculated as follows

$$d_{major} = \sqrt{\frac{d_x^2 + d_y^2}{2} + \sqrt{\left(\frac{d_x^2 - d_y^2}{2}\right)^2 + d_{xy}^2}} \ . \tag{11}$$

d_x^2, d_y^2 and d_{xy} are the error variances in the direction of the x and y axis, and covariance between the x and y, respectively. They are calculated by propagating the measurement variances through the measurement model as shown in Equation 12. Given that the measurement model is linearised, the geometry between the user and the GNSS/LPS is known, and the measurement errors are assumed to be Gaussian, errors can be propagated without knowledge of the estimated position.

$$\begin{aligned} d_x^2 &= \sum_{i=1}^{N_S} s_{1,i}^2 \sigma_S^2 + \sum_{j=1}^{N_I} s_{1,j}^2 \sigma_I^2 \\ d_y^2 &= \sum_{i=1}^{N_S} s_{2,i}^2 \sigma_S^2 + \sum_{j=1}^{N_I} s_{2,j}^2 \sigma_I^2 \\ d_{xy} &= \sum_{i=1}^{N_S} s_{1,i} s_{2,i} \sigma_S^2 + \sum_{j=1}^{N_I} s_{1,j} s_{2,j} \sigma_I^2 \end{aligned} \tag{12}$$

$s_{1,i}$ and $s_{2,i}$ are x and y elements of the S matrix which is calculated as

$$S = \left(H_k^T W H_k\right)^{-1} H_k^T W \ . \tag{13}$$

Matrix H_k is a measurement matrix which 'describes' the geometry between the dynamic user and satellites, and between the dynamic user and LPS. It is defined in the previous section. W is the weighting matrix with measurement variances as diagonal elements. In this paper W is defined as

$$\underset{(N_S+N_I)\times(N_S+N_I)}{W} = \begin{bmatrix} \sigma_{S,i}^2 & 0 & 0 & 0 & 0 & 0 \\ 0 & \ddots & 0 & 0 & 0 & 0 \\ 0 & 0 & \sigma_{S,N_S}^2 & 0 & 0 & 0 \\ 0 & 0 & 0 & \sigma_{I,j}^2 & 0 & 0 \\ 0 & 0 & 0 & 0 & \ddots & 0 \\ 0 & 0 & 0 & 0 & 0 & \sigma_{I,N_I}^2 \end{bmatrix}. \tag{14}$$

The presented algorithm is tailored for multi-sensor fusion. However, in case of HPL estimation for stand-alone GNSS solution, terms in Equation 12 relating to the LPS become equal to zero, and rows in matrices H_k and W are removed. The same applies to LPS only solution. The estimated HPL is proportional to the Horizontal Dilution Of Precision (HDOP) which is often used in geomatics to quantify the network geometry quality. In case of GNSS data, network geometry refers to the observed satellite geometry. HDOP is calculated as,

$$R = \left(H_k^T H_k \right)^{-1}$$
$$HDOP = \sqrt{\sigma_{R,x}^2 + \sigma_{R,y}^2}. \quad (15)$$

$\sigma_{R,x}^2$ and $\sigma_{R,y}^2$ denote the elements of R matrix related to the x and y coordinates.

4. RESULTS AND DISCUSSION

This section presents the results of the experiments carried out using the data collected in different environments for the EKF and RAIM algorithms. Firstly, the performance of stand-alone GPS data is tested. Then, the simulated relative ranges measured to the simulated LPS are used for producing the multi-sensor fusion results. The performance for both data sets is tested when the vehicle is static in the open-sky environment, and dynamic in four types of environment: highway, open-sky area, suburb area and urban-canyon.

Process noise and measurement noise are assumed to be Gaussian with zero-mean. The standard deviation of the acceleration noise is *1 ms*$^{-2}$. The clock bias noise is assumed to have the standard deviation of *1 m.* GPS pseudorange standard deviation is *5.1 m* and for simulated relative ranges is *1 m*. Based on the requirements for payment-critical applications specified in European GNSS agency's report from 2015, Horizontal AL (HAL) of *20 m* is chosen with the required integrity risk of *1·10*$^{-5}$. Position and integrity estimate are available every 0.05 s (i.e., 20 Hz).

4.1 Integrity monitoring results for GPS data collected in different environments

The integrity performance results are shown on a Stanford diagram (more in Zhu *et al.*, 2018). Stanford diagrams classify the integrity assessment in five different groups: nominal operations, misleading operations, hazardously misleading operations, system unavailable and misleading information, and system unavailable. These classifications are based on the fulfilment of the requirements that the estimated Horizontal Positioning Error (HPE) needs to be within the HPL which cannot be larger than the HAL.

Table 1 shows the simple statistics calculated for the estimated HPL and HPE values for every environment considered in this paper.

[m]	Static vehicle	Highway	Open sky	Suburbs	Urban canyon
Average HPL	17.5	19.3	25.1	32.7	43.1
Stand. deviation	0.01	2.7	3.3	15.9	22.2
Min HPL	17.5	17.5	23.8	23.1	19.6
Max HPL	17.6	35.6	51.5	129.7	133.4
Average HPE	2.7	2.6	2.6	3.1	39.1
Stand. deviation	0.4	3.3	0.3	1.5	59.5
Max HPE	3.5	18.2	5.0	34.1	366.9

Table 1. Average HPL and standard deviation, minimum and maximum of HPL as well as the average 2D error (i.e., HPE) and HPE standard deviation, minimum and maximum value. All values are calculated based on the GPS data for different environments.

Firstly, the performance of the static vehicle GPS data set is shown (see Figure 5). Figure 5a

shows that 100% of the time, integrity monitoring algorithm has correctly classified integrity as available (i.e., nominal operations). As said in the previous section, HPL is proportional to the network geometry. Given that the vehicle was static for a short period of time (under 2 min), the geometry of satellites was not changing which has resulted in a stable HPL assessment. Figure 5b shows the HAL and HPE (i.e., 2D error) along the timeline of the experiment. On average, HPL was estimated to be 17.5 m with a probability of failure $1 \cdot 10^{-5}$ (see Table 1).

Data collection on the highway lasted for around 12 min. During the data collection, the HPE has never surpassed the HAL. However, HPL did exceed the HAL 27% of the time which has resulted in integrity unavailability. 73% of the time, integrity was correctly classified as available (see Figure 6a). Figure 6b shows the variation in estimated HPL from 17.5 m to about 30 m. This variation probably happens due to the change in geometry between the vehicle and GPS satellites. Table 1 shows that the maximum estimated HPL was around 36 m. The average HPL is 19 m with the standard deviation of almost 3 m.

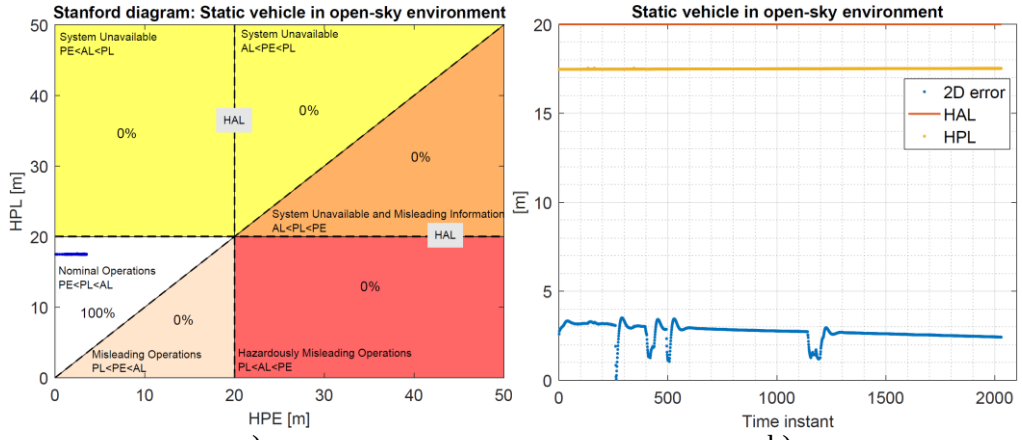

Figure 5. Integrity monitoring results for a static vehicle in an open-sky environment. a) Stanford diagram with integrity assessment. b) Timeline of HPL and 2D error estimation compared to HAL.

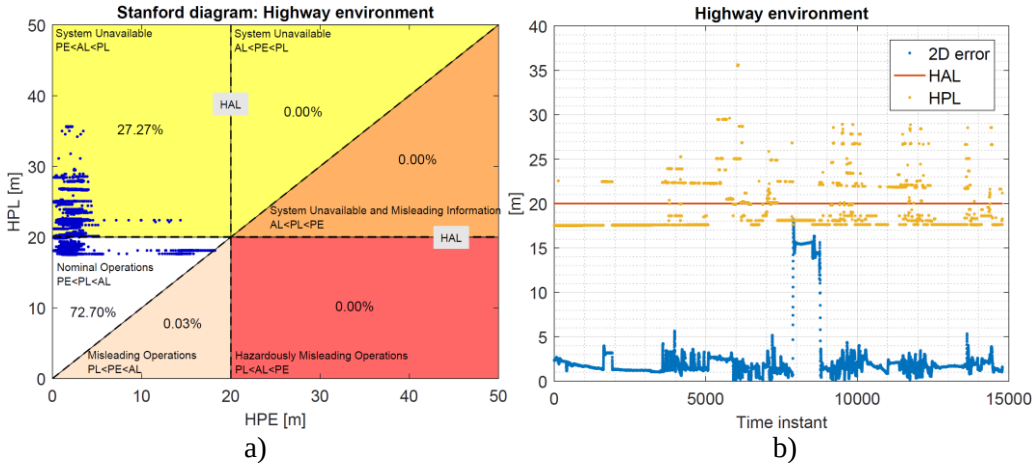

Figure 6. Integrity monitoring results for a vehicle on a highway. a) Stanford diagram with integrity assessment. b) Timeline of HPL and 2D error estimation compared to HAL.

Figure 7a shows the Stanford diagram for the open-sky environment where the vehicle's position integrity was unavailable 100% of the time. Although the average HPE was the same as for the static or highway data, the estimated HPL was always larger than the required HAL. Further explanation on this will be made at the end of this section. Figure 7b shows the

change of HPL and HPE along the timeline (about 8 min of data). In comparison to the highway data, it seems that although worse, the geometry in the open-sky environment was more stable. The average estimated HPL is 25 m with the standard deviation of 3 m due to the presence of the large HPL estimates from 30 m to 50 m (see Table 1).

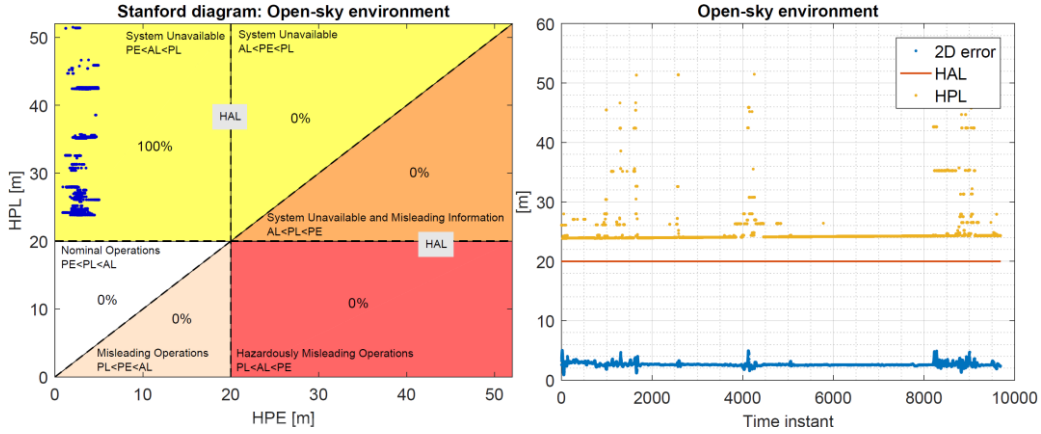

a) b)

Figure 7. Integrity monitoring results for a vehicle in an open-sky environment. a) Stanford diagram with integrity assessment. b) Timeline of HPL and 2D error estimation compared to HAL.

Figure 8a shows the integrity availability for the suburban environment. Here, integrity was unavailable 100% of the time. It should be noted that in 11.5 min of data collection with the frequency of 20 Hz, five time instances occurred where less than five measurements were available. Thus, in those cases, integrity was automatically classified as unavailable. Figure 8b shows the HPL and HPE along the timeline of the data collection. In this graph, a differentiation is made between the positions estimated when less than five measurements are available and when five or more are available. The same is done for the HPL estimate. Yellow dots show the missing HPL estimations (when the number of measurements is less than five). Note that their values are not 140 m since the value does not exist as it cannot be estimated. Table 1 shows that the average HPL is 33 m with the standard deviation of 16 m. Maximum estimated HPL is 130 m. However, looking at the Figure 8b, the results seem to be similar to the results in the open-sky environment where a clear limit below which there are no HPL estimations is visible, and the increases occur when the geometry changes.

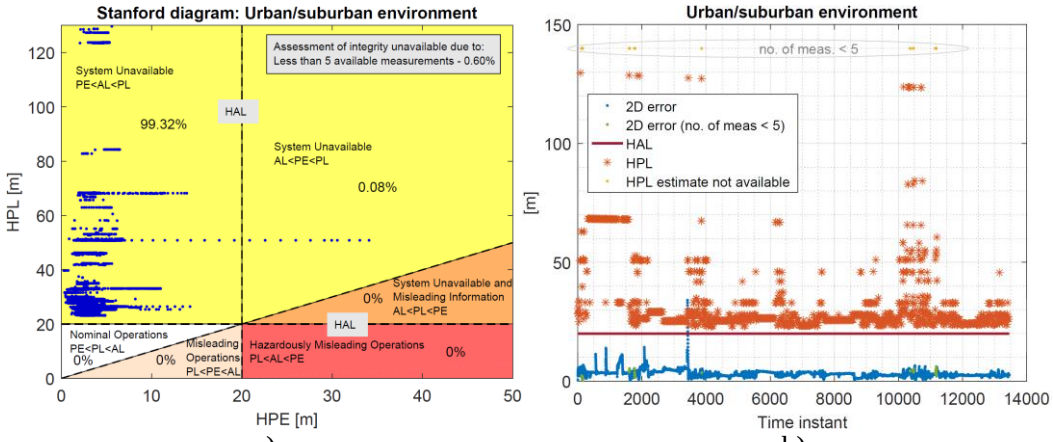

a) b)

Figure 8. Integrity monitoring results for a vehicle in a suburban environment. a) Stanford diagram with integrity assessment. b) Timeline of HPL and 2D error estimation compared to HAL.

Finally, the results for data collected in the urban canyon are shown in Figure 9. Here, 49% of

the time, the integrity was not available due to lack of measurements for HPL calculation. Thus, even before the integrity is calculated, 49% of positions automatically do not have integrity assessment available. As shown in Figure 9a, an additional 43% of positions do not have integrity available due to HPL exceeding HAL. 1% of the time the integrity is correctly classified as available. Figure 9b shows that this occurs at the end of the 7 min data collection. When the HPL assessment is available, it is on average equal to 43 m with the standard deviation of 22 m. Maximum estimated HPL is similar to the one in the suburban environment. Unlike all the other environments where the HPE is similar, in urban canyon average HPE is around 39 m.

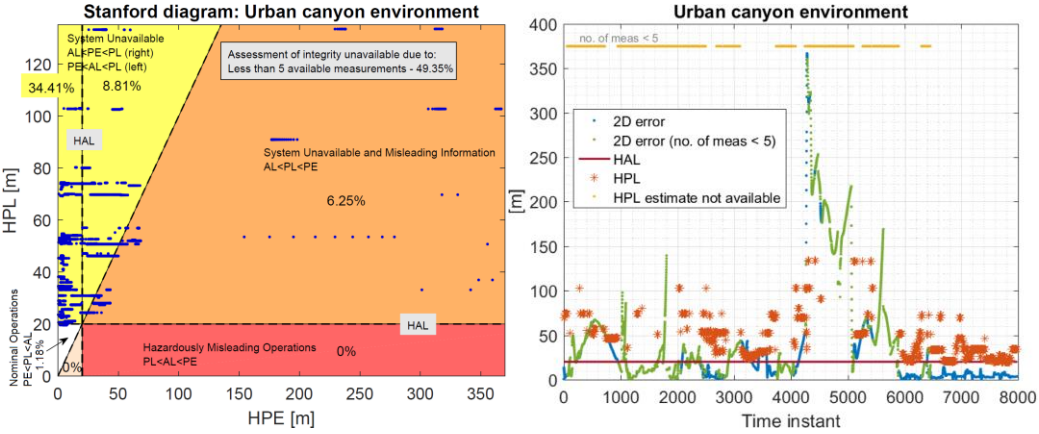

a) b)

Figure 9. Integrity monitoring results for a vehicle in an urban canyon. a) Stanford diagram with integrity assessment. b) Timeline of HPL and 2D error estimation compared to HAL.

Figure 10 shows the GPS pseudorange availability for all experiments. Here, it can be seen that when the vehicle is static the geometry between the vehicle and the GPS satellites is stable, not only due to the short data collection, but more importantly because the number of pseudoranges does not change. When the vehicle is on the highway, it was shown that the HPL estimate changes which implies that the geometry between the vehicle and the satellites changes repeatedly. This can be explained with the changing number of available measurements which affects the geometry. These changes could occur due to numerous trees and viaducts on the route where the vehicle was driving (Figure 1). The integrity was unavailable 100% of the time in the open-sky environment. It was expected that the performance and measurement availability in the open-sky environment would be the best. However, the maximum number of relative ranges measured in open-sky was 10 in comparison to the highway where it was 13. After the sky plots and satellite elevations were checked, three satellites were identified which have had low elevation (about 5˚) during the data collection on the highway, and their elevation was dropping. By the time the vehicle arrived to the open-sky environment, those three satellites were no longer visible. Thus, the minimum HPL estimate was shifted. Furthermore, change in the number of measurements coincides with the changes in the HPL estimate in Figure 7b. The same can be said for the suburban environment with a difference in the number of changes of the measurement availability and the HPL estimates. Finally, the biggest changes of both the measurements and the HPL happen in the urban canyon. As expected, the most probable cause of this is the local environment causing the measurement unavailability and presence of more error sources (i.e., multipath from buildings). The reason why integrity is available 1% of the time at the end of the urban canyon experiment can be seen in the highest number of available measurements in the experiment which occurs because the vehicle at that point gets out of urban canyons (see Figure 4, the south portion of the trajectory).

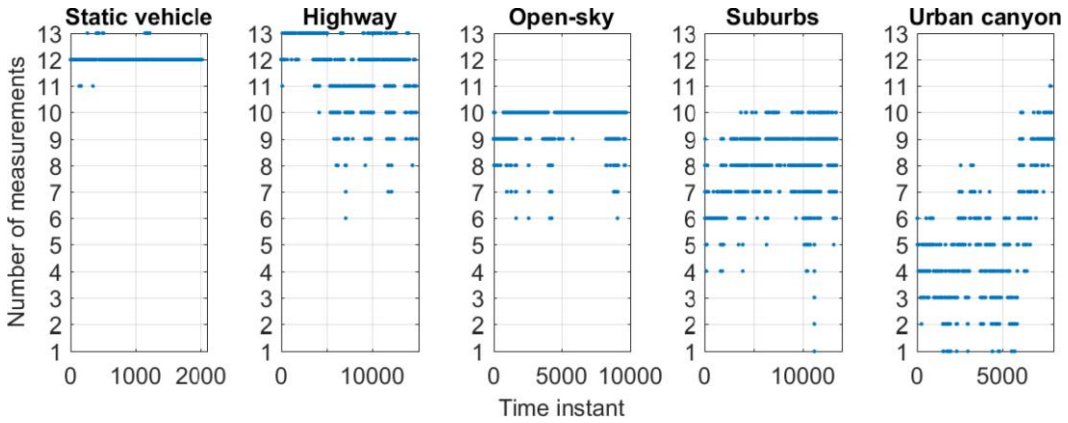

Figure 10. Availability of GPS satellites in different environments.

4.2 Integrity monitoring results for multi-sensor data in different environments

The previous section has shown the dependence of the WLS RAIM algorithm on the environment of the user when it is based solely on the GPS data. Here, simulated relative ranges are fused with GPS data and the effect of that fusion is discussed in this section.

It should be noted that this comparison was only made on the portions of the data where LPS anchors were simulated (see Figures 1-4). Thus, the percentages in Figure 11 will be different from the integrity levels shown in the previous section.

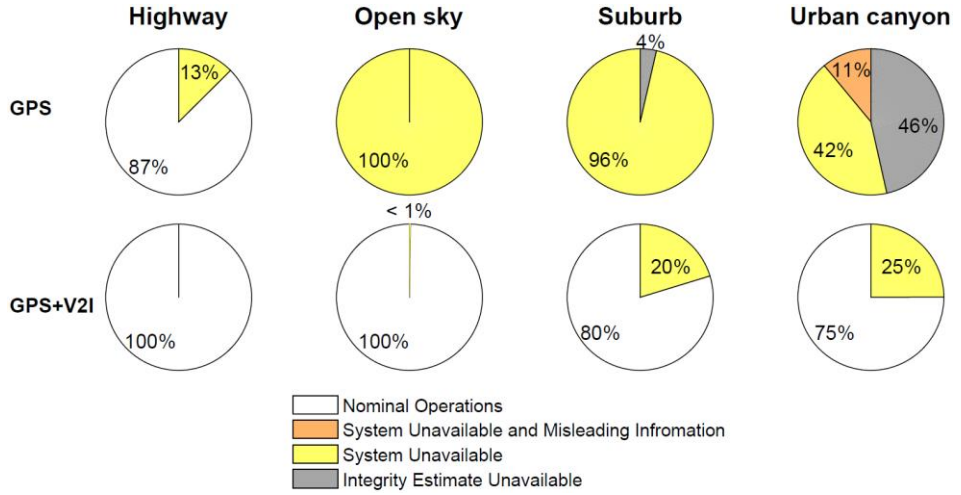

Figure 11. Comparison of the integrity availability estimates for positioning systems based on GPS only (top row) and GPS+V2I (bottom row) data. Integrity estimate is compared for all four different environments: highway, open sky, suburb and urban canyon environment.

As hypothesised, the LPS has significantly improved the rate of integrity availability. Furthermore, the rates of integrity availability are similar and seem to depend on the environment less than they used to. Figure 11 compares the integrity availability assessments for four environments where the vehicle was dynamic. The performance of GPS data is shown in the first row and the GPS+V2I data is shown in the second row (V2I or Vehicle-to-Infrastructure refers to the relative ranges measured to LPS). As shown, for highway and open-sky environment the availability grows to the same level – 100%. Due to the fusion of

GPS with LPS measurements, unavailability of integrity estimate (due to lack of measurements) is completely removed for both the suburban and urban canyon environments. Now, integrity is available 80% and 75% of the time in the suburban and urban canyon environment, respectively. Levels of integrity unavailability are probably still present in the suburban and urban canyon environment because of the bad GPS data. The improvement in HPL and HPE for all environment types is numerically shown in Table 2.

	Highway		Open-sky		Suburb		Urban canyon	
	GPS	GPS+V2I	GPS	GPS+V2I	GPS	GPS+V2I	GPS	GPS+V2I
HPL [m]	18.4	9.7	24.2	7.7	42.8	14.8	45.0	16.7
HPE [m]	1.8	0.5	2.6	0.3	3.0	0.7	16.6	1.0

Table 2. Average HPL and HPE calculated based on the GPS only and GPS+V2I data. The values are calculated for the subset of GPS data where V2I data were simulated.

5. CONCLUSIONS

The main goal of the paper was to determine the effect of different environments on stand-alone GPS data integrity availability. It was demonstrated that the integrity deteriorates as the environment becomes more challenging due to decrease in measurement availability and observed satellite geometry quality as well as the probable presence of the multipath. It is demonstrated that fusion with the LPS relative ranging data improves the position estimate accuracy to sub-meter levels as well as the integrity availability levels. More importantly, it has been demonstrated that the integrity availability levels become similar in different environments (100% for highway and open-sky environments and around 75% for suburban and urban canyon environments). Thus, the effect of different environments on integrity estimate was mitigated through multi-sensor solution. This is significant as the goal of designing the integrity monitoring algorithm for the urban environment should be to minimise the environment effects. However, given the use of simulated relative ranging data, these results may be optimistic due to relative ranges not being under the influence of the local environment in terms of multipath and measurement availability. Nevertheless, this paper has demonstrated the need for multi-sensor fusion integrity monitoring algorithms since the stand-alone GPS does not offer an adequate level of integrity necessary for different ITS applications.

The performance of the used RAIM indicated a few issues in terms of its applicability in urban environments. RAIM algorithms are only able to estimate integrity when five or more measurements are available, even if the positioning system is still able to estimate positions. This issue has been highlighted during the urban-canyon experiment where, by default integrity was unavailable almost 50% of the time. This conclusion would not change even if multi-GNSS data were used as the GLONASS and Galileo data would probably be unavailable as well. Furthermore, HPL is proportional to the geometry between the user and the nodes. Thus, any change in geometry causes a change in the value of estimated HPL even if the accuracy is not significantly affected by the change in geometry. Issue of changing geometry is highlighted across all the experiments. Change of measurement availability also affects the estimated HPL since the change in the number of measurements effectively changes the geometry. Thus, using the available multi-GNSS data would have improved the HPL estimate (especially in the open-sky environment). Lastly, given that the hazardously

misleading information never occurred (even when estimated HPE exceeds 100 m) it could be concluded that the algorithm is too conservative and thus, even in good conditions experiences high integrity unavailability rates. All these issues are not surprising given the fact that algorithms like the one presented in this paper were originally designed for civil aviation which operates in a completely different environment from the environment a road user operates in. ITS applications would benefit from the integrity monitoring algorithms that are less dependent of the measurement availability and not proportional to the network geometry as those things are the most affected in the urban environment. The future work will focus on multi-sensor fusion integrity monitoring which has shown promising results in this paper.

REFERENCES

Brown AK (1988) Civil Aviation Integrity Requirements for the Global Positioning System, *Navigation: Journal of the Institute of Navigation*, 35(1): 23-40.

Bruckner DC (2010) On the treatment of noise and conspiring bias in dual-frequency differential global navigation satellite systems, *Ph.D. Thesis*, the School of Electrical Engineering and Computer Science and the Russ College of Engineering and Technology of Ohio University, Athens, Ohio, USA.

El-Mowafy A, Kubo N (2017) Integrity monitoring of vehicle positioning in urban environment using RTK-GNSS, IMU and speedometer, *Measurement Science and Technology* 28(2017) 055102 (12pp).

El-Mowafy A, Kubo N (2018) Integrity monitoring for Positioning of intelligent transport systems using integrated RTK-GNSS, IMU and vehicle odometer, *IET Intelligent Transport Systems* 12(8): 901 –908.

European GNSS Agency (2015) Report on the Performance and Level of Integrity for Safety and Liability Critical Multi-Applications, *European GNSS Agency report*, available online: https://www.gsa.europa.eu/sites/default/files/calls_for_proposals/Annex%202.pdf (accessed: 8 Dec 2019)

Gabela J, Goel S, Kealy A, Hedley M, Moran W and Williams A (2018) Cramèr Rao Bound Analysis for Cooperative Positioning in Intelligent Transportation Systems, *Proceedings of the International Global Navigation Satellite Systems Association - IGNSS Symposium 2018*, Sydney, Australia.

Gabela J, Kealy A, Li S, Hedley M, Moran W, Ni W, Williams S (2019) The Effect of Linear Approximation and Gaussian Noise Assumption in Multi-Sensor Positioning Through Experimental Evaluation, *IEEE Sensors Journal* 19(22): 10719-10727.

Kealy A, Retscher G, Toth C, Hasnur-Rabiain A, Gikas V, Grejner-Brzezinska D, Danezis C, Moore T (2015) Collaborative Navigation as a Solution for PNT Applications in GNSS Challenged Environments – Report on Field Trials of a Joint FIG / IAG Working Group, *Journal of Applied Geodesy*, 9(4): 244–263.

Leica Geosystems AG, Leica Viva GNSS GS15 receiver Datasheet, url: https://w3.leica-geosystems.com/downloads123/zz/gpsgis/viva%20gs15/brochures-datasheet/leica_viva_gs15_ds_en.pdf (last accessed on November 11th, 2019).

Salós D, Martineau A, Macabiau C, Bonhoure B, Kubrak D (2014) Receiver Autonomous Integrity Monitoring of GNSS Signals for Electronic Toll Collection, IEEE Transactions on Intelligent Transportation Systems, 15(1): 94-103.

Shytermeja E, Garcia Peña AJ, Julien O (2014) Proposed architecture for integrity monitoring of a GNSS/MEMS system with a Fisheye camera in urban environment, Proceedings of the IEEE International Conference on Localization and Global Navigation Satellite Systems - ICL-GNSS

2014, Helsinki, Finland.

Smith E, Knight M, Dempster A, Cheong JW (2018) Integrity Capability of Standalone GPS, *Proceedings of the International Global Navigation Satellite Systems Association - IGNSS Symposium 2018*, Sydney, Australia.

Tran HT, Lo Presti L (2019) Kalman filter-based ARAIM algorithm for integrity monitoring in urban environment, *Information & Communications Technology Express*, 5(1): 65-71.

Zhu N, Marais J, Bétaille D, Berbineau M (2018) GNSS Position Integrity in Urban Environments: A Review of Literature, *IEEE Transactions on Intelligent Transportation Systems*, 19(9): 2762-2778.